# CMOS-compatible optical switching concept based on strain-induced refractive-index tuning

**Michele Virgilio,[1,2,*] Bernd Witzigmann,[3] Gabriele Bolognini,[4] Subhajit Guha,[5] Thomas Schroeder,[5] and Giovanni Capellini[5,6]**

[1]*Dip. di Fisica "E. Fermi", Università di Pisa, Largo Pontecorvo 3, 56127 Pisa, Italy*
[2]*NEST, Istituto Nanoscienze-CNR, P.za San Silvestro 12, 56127 Pisa, Italy*
[3]*Kassel University and CINSaT, Wilhelmshöher Allee 71, 34121 Kassel, Germany*
[4]*Consiglio Nazionale delle Ricerche, IMM Institute, 40129 Bologna, Italy*
[5]*IHP, Im Technologiepark 25, 15236 Frankfurt (Oder), Germany*
[6]*Dipartimento di Scienze, Università Roma Tre, Viale Marconi 446, 00146 Rome, Italy*
[*]*virgilio@df.unipi.it*

**Abstract:** In this paper we present a planar lightwave switching mechanism based on large refractive index variations induced by electrically-driven strain control in a CMOS-compatible photonic platform. Feasibility of the proposed concept, having general validity, is numerically analyzed in a specific case-study given by a Mach-Zehnder Interferometer with Ge waveguides topped by a piezoelectric stressor. The stressor can be operated in order to dynamically tune the strain into the two interferometric arms. The strain modifies the Ge band structure and can induce refractive index variations up to 0.05. We demonstrate that this approach can enable ultra-compact devices featuring low loss propagation for light wavelengths below the waveguide band gap energy, high extinction ratios (>30 dB) and low intrinsic insertion losses (2 dB). The operation wavelength can be extended in the whole FIR spectrum by using SiGe(Sn) alloy waveguides.

©2015 Optical Society of America

**OCIS codes:** (130.4815) Optical switching devices; (160.6000) Semiconductor materials; (130.0130) Integrated optics

## References and links

1. L. Vivien and L. Pavesi, eds., *Handbook of Silicon Photonics*, (Taylor and Francis, 2013).
2. A. Liu, R. Jones, L. Liao, D. Samara-Rubio, D. Rubin, O. Cohen, R. Nicolaescu, and M. Paniccia, "A high-speed silicon optical modulator based on a metal-oxide-semiconductor capacitor," Nature **427**(6975), 615–618 (2004).
3. G. T. Reed, G. Mashanovich, F. Y. Gardes, and D. J. Thomson, "Silicon optical modulators," Nat. Photonics **4**(8), 518–526 (2010).
4. P. Dong, S. Liao, D. Feng, H. Liang, D. Zheng, R. Shafiiha, C. C. Kung, W. Qian, G. Li, X. Zheng, A. V. Krishnamoorthy, and M. Asghari, "Low $V_{pp}$, ultralow-energy, compact, high-speed silicon electro-optic modulator," Opt. Express **17**(25), 22484–22490 (2009).
5. R. S. Jacobsen, K. N. Andersen, P. I. Borel, J. Fage-Pedersen, L. H. Frandsen, O. Hansen, M. Kristensen, A. V. Lavrinenko, G. Moulin, H. Ou, C. Peucheret, B. Zsigri, and A. Bjarklev, "Strained silicon as a new electro-optic material," Nature **441**(7090), 199–202 (2006).
6. M. Cazzanelli, F. Bianco, E. Borga, G. Pucker, M. Ghulinyan, E. Degoli, E. Luppi, V. Véniard, S. Ossicini, D. Modotto, S. Wabnitz, R. Pierobon, and L. Pavesi, "Second-harmonic generation in silicon waveguides strained by silicon nitride," Nat. Mater. **11**(2), 148–154 (2012).
7. B. Chmielak, M. Waldow, C. Matheisen, C. Ripperda, J. Bolten, T. Wahlbrink, M. Nagel, F. Merget, and H. Kurz, "Pockels effect based fully integrated, strained silicon electro-optic modulator," Opt. Express **19**(18), 17212–17219 (2011).
8. B. Chmielak, C. Matheisen, C. Ripperda, J. Bolten, T. Wahlbrink, M. Waldow, and H. Kurz, "Investigation of local strain distribution and linear electro-optic effect in strained silicon waveguides," Opt. Express **21**(21), 25324–25332 (2013).
9. N. Andriolli, I. Cerutti, P. Pintus, M. Scaffardi, D. Marini, G. B. Montanari, F. Mancarella, M. Ferri, R. Balboni, and G. Bolognini, "Challenges and progress toward a silicon-based multi-microring optical network-on-chip," in Proceedings of IEEE European Conference on Networks and Communications, pp. 1–5 (2014).
10. V. Kaman, R. J. Helkey, and J. E. Bowers, "Compact and scalable three-dimensional microelectromechanical system optical switches," J. Opt Network. **6**(1), 19–24 (2007).

#230620 - $15.00 USD Received 11 Dec 2014; revised 30 Jan 2015; accepted 4 Feb 2015; published 25 Feb 2015
© 2015 OSA

11. B. G. Lee, A. Biberman, J. Chan, and K. Bergman, “High-performance modulators and switches for silicon photonic networks-on-chip,” IEE J. Sel. Top. Quantum Electron. **16**(1), 6–22 (2010).
12. R. A. Soref, “Mid-infrared photonics in silicon and germanium,” Nat. Photonics **4**(8), 495–497 (2010).
13. G. Roelkens, U. Dave, A. Gassenq, N. Hattasan, C. Hu, B. Kuyken, F. Leo, A. Malik, M. Muneeb, E. Ryckeboer, Z. Hens, R. Baets, Y. Shimura, F. Gencarelli, B. Vincent, R. Loo, J. Van Campenhout, L. Cerutti, J.-B. Rodriguez, E. Tournié, X. Chen, M. Nedeljkovic, G. Z. Mashanovich, L. Shen, N. Healy, A. C. Peacock, X. Liu, R. Osgood, and W. J. Green, “Silicon-based photonic integration beyond the telecommunication wavelength range,” IEEE J. Sel. Top. Quantum Electron. **20**(4), 8201511 (2014).
14. P. Boucaud, M. El Kurdi, A. Ghrib, M. Prost, M. de Kersauson, S. Sauvage, F. Aniel, X. Checoury, G. Beaudoin, L. Largeau, I. Sagnes, G. Ndong, M. Chaigneau, and R. Ossikovski, “Recent advances in germanium emission,” Photon. Res. **1**(3), 102–109 (2013).
15. G. Sun, R. A. Soref, and H. H. Cheng, “Design of a Si-based lattice-matched room-temperature GeSn/GeSiSn multi-quantum-well mid-infrared laser diode,” Opt. Express **18**(19), 19957–19965 (2010).
16. D. Knoll, S. Lischke, L. Zimmermann, B. Heinemann, D. Micusik, P.Ostrovskyy, G. Winzer, M. Kroh, R. Barth, T. Grabolla, K. Schulz, M.Fraschke, M. Lisker, J. Drews, A. Trusch, A. Krüger, S. Marschmeyer, H. H. Richter, O. Fursenko, Y. Yamamoto, B. Wohlfeil, K. Petermann, A. Beling, Q.Zhou, and B. Tillack, “Monolithically Integrated 25Gbit/sec Receiver for 1.55 μm in Photonic BiCMOS Technology”, Optical Fiber Communications (OFC2014) Conference Digest, Optical Society of America, paper Th4C. 4.1–3, (2014).
17. M. D. Nguyen, H. N. Vu, D. H. A. Blank, and G. Rijnders, “Epitaxial $Pb(Zr,Ti)O_3$ thin films for a MEMS application,” Adv. Nat. Sci. Nanosci. Nanotechnol. **2**(1), 015005 (2011).
18. D. Isarakorn, A. Sambri, P. Janphuang, D. Briand, S. Gariglio, J.-M. Triscone, F. Guy, J. W. Reiner, C. H. Ahn, and N. F. de Rooij, “Epitaxial piezoelectric MEMS on silicon,” J. Micromech. Microeng. **20**(5), 055008 (2010).
19. D. S. L. Pontes, L. Gracia, F. M. Pontes, A. Beltran, J. Andres, and E. Longo, “Synthesis, optical and ferroelectric properties of PZT thin films: experimental and theoretical investigation,” J. Mater. Chem. **22**(14), 6587–6596 (2012).
20. I. Y. Shen, G. Z. Cao, C. Wuc, and C. Lee, “PZT Thin-Film Meso- and Micro Devices,” Ferroelectrics **342**, 15–34 (2006).
21. M. Ghasemi-Nejhad, S. Pourjalali, M. Uyema, and A. Yousefpour, “Finite Element Method for Active Vibration Suppression of Smart Composite Structures using Piezoelectric Materials,” J. Thermopl. Comp. Mater. **19**(3), 309–352 (2006).
22. M. Virgilio, C. L. Manganelli, G. Grosso, G. Pizzi, and G. Capellini, “Radiative recombination and optical gain spectra in biaxially strained *n*-type germanium,” Phys. Rev. B **87**(23), 235313 (2013).
23. M. Virgilio and G. Grosso, “Optical spin orientation in strained Ge/SiGe quantum wells: A tight-binding approach,” Phys. Rev. B **80**(20), 205309 (2009).
24. F. Römer and B. Witzigmann, “Spectral and spatial properties of the spontaneous emission enhancement in photonic crystal cavities,” J. Opt. Soc. Am. B **25**(1), 31–40 (2008).
25. R. A. Soref and B. R. Bennet, “Electrooptical effects in silicon,” IEEE J. Quantum Electron. **23**(1), 123–129 (1987).
26. G. Capellini, C. Reich, S. Guha, Y. Yamamoto, M. Lisker, M. Virgilio, A. Ghrib, M. El Kurdi, P. Boucaud, B. Tillack, and T. Schroeder, “Tensile Ge microstructures for lasing fabricated by means of a silicon complementary metal-oxide-semiconductor process,” Opt. Express **22**(1), 399–410 (2014).
27. G. Lifante, *Integrated Photonics: Fundamentals* (Wiley, 2003), Chap. 3.

## 1. Introduction

Optical switching is one of the most important functional building blocks in the current telecom and datacom domains (together with light intensity modulation and phase modulation), and the development of highly-integrable, low-power consumption optical devices enabling efficient switching is of paramount importance in future systems and networks. The major obstacle to achieve efficient basic light wave signal processing with silicon is given by the vanishing electro-optic tensor related to its center-symmetric property. Boosted by the urge for fast operating opto-electronic circuitry integrated on silicon technology, alternative approaches to light switching (and light modulation in general) with Si-based materials have been recently proposed to overcome this limitation. The operating principles rely either on the electrical modulation of the absorption coefficient $\alpha$, called electroabsorption modulation, or of the real part of the refractive index $n_1$, known as interferential modulation (see a recent review in [1]). In the latter case, optical switching at various device ports is achieved tuning the intensity variations resulting from the self-interference of the incoming beam in suitably designed photonic structures, e.g. a Mach-Zehnder interferometer (MZI) [2]. In these devices the phase difference is controlled by modulating the refractive index via carrier injection/depletion in one or both the

#230620 - $15.00 USD Received 11 Dec 2014; revised 30 Jan 2015; accepted 4 Feb 2015; published 25 Feb 2015
© 2015 OSA

interferometric arms. The main drawback of this approach is that a complete destructive interference requires a phase mismatch which is often achievable only with very long optical paths (~1 mm using carrier depletion), due to the relatively low variation of the refractive index value ($\sim 10^{-3}$). Moreover, the consequently large footprint ($10^3$-$10^4$ $\mu m^2$) typically involves large power consumption ($10^3$-$10^4$ fJ/bit) and large insertion losses (~10 dB). Shorter optical paths (in the few hundred μm range) can be achieved employing carrier injection, which is however also characterized by relatively high loss/consumption values. Energy efficiency is a critical limit also for the performance of interferometric modulators based on the thermo-optical effect [3]. Much more compact devices relying on disk or ring geometries have been recently demonstrated in [4], albeit at the expenses of limited operation wavelength width (<1 nm) and modulation depth (<10 dB).

In the past few years, the use of strain in silicon has shown promising features for achieving effective light wave signal processing on a CMOS compatible platform. Strained silicon is obtained combining intrinsic and extrinsic effects with geometry (e.g. through doping or film deposition above suitable nanostructures). In particular, it has recently been observed that a stressor layer on top of a silicon waveguide can effectively break the silicon lattice inversion symmetry resulting in a non-vanishing linear electro-optic effect [5] or nonlinear effects such as second-harmonic generation [6]. Indeed, signal intensity modulation has recently been achieved in strained-Si MZI structures albeit their performance seems still to be limited by the moderate refractive index variations. In fact, with a rather high applied electrode potential $V_{mod}$ = 30 V, $\Delta n$ is of the order of $2 \times 10^{-5}$ [7], resulting in interference $V_\pi L_\pi$ values in excess of ~90 V·cm [8], $V_\pi$ and $L_\pi$ being the $\pi$-dephasing voltage and length, respectively. An innovative CMOS-compatible mechanism enabling refractive index variation and light wave signal processing with small footprint and high integrability can then foster the development of a range of integrated devices.

Here we propose a novel scheme to obtain significant strain-induced refractive index variations, leading to large phase shifts with very small form factors and enabling optical switching with rates up to 0.5 GHz, with an inherently transparent behavior to modulation formats and bit rates of incoming light wave signals. The possible range of applications can encompass domains where compactness becomes a mandatory feature, e.g. in optical switches for signal routing in circuit- or packet-switched networks for telecom (e.g. for future networks-on-chip in large data center infrastructures) [9].

Actually, for large data centers in particular, strict constraints are imposed on the photonic switch matrices by the very large port number, the high total data throughput, and the wide bandwidth per port. On the other hand, switching-rate constraints are not extremely stringent in typical circuit-switching schemes (rates can be as low as a fraction of kHz). It is worth to notice that optical switches based on current micro electro-mechanical system (MEMS) technology can be employed for inter-board interconnections in such a domain, although their use is characterized by the presence of moving parts as well as by challenges related to trade-offs in parameters such as cross-talk versus scalability [10]. Furthermore, the use of MEMS-switches is severely hindered for other interconnection networks such as on-chip as well as off- chip (or intra-board) interconnections [11]. In order to handle hundreds of input/output large-bandwidth ports, not easily manageable by traditional electrical switching schemes, extremely small device form factors are mandatory.

In order to assess the proposed refractive-index variation mechanism, whose validity extends beyond the application examples given in this paper, we use Ge waveguides (WG), whose refractive index is varied by means of a tunable, electrically actuated stressor. Germanium is a CMOS-compatible material which is transparent in the near infrared range and allows for a strong confinement of the guided light [12]. Furthermore, as clarified in the following, its band structure and the way it can be modified by a stressor is particularly suitable to implement the proposed operating principle.

#230620 - $15.00 USD Received 11 Dec 2014; revised 30 Jan 2015; accepted 4 Feb 2015; published 25 Feb 2015
© 2015 OSA

We numerically investigate the performance of a case-study device, given by a Mach-Zehnder interferometer (MZI) operating with an electrically actuated stressor layer deposited on top of the Ge WG operating in the near infrared range. Such a spectral region, which comprises and extends beyond the C- and L-telecom bands, has recently attracted a vast interest [13] owing to the forthcoming availability of integrated light emitting sources operating therein, such as tensile Ge-based [14] or GeSn-based [15] lasers.

For optimized structures, designed to have a low footprint of the effective switching region ($<10^2$ μ$m^2$), we predict very high extinction ratios (> 30 dB), very low insertion losses (~1 dB), and relatively low operation peak-to-peak voltage (2-10 V). Beside the conditions of the discussed case-study, the validity of our approach is more general. As a matter of fact, optical switching systems based on photonic integrated circuits (PICs), typically features complex architectures comprising micro-ring devices, photonic crystal structures, etc., in addition to MZIs, and to the opto-electronic driving/control circuitry. Our proposed mechanism can also be applied to all above-mentioned building blocks, and, considering the ~ × 10 fold increase of the refractive index variation achievable with respect to standard techniques, bringing about a performance improvement to the whole system.

Finally, the proposed principle can be applied to a much broader range of CMOS-compatible materials (e.g. SiGeSn or Ge-rich SiGe-based waveguides), thus extending also the spectral range of interests.

## 2. Case-study device geometry and methods

The feasibility of the proposed concept is assessed on a specific CMOS-compatible device, given by a symmetric-arm MZI structure in which the light travels in waveguides made of (001)-oriented (*z* axis) Ge crystal, directly fabricated on-top of a silica layer (see Fig. 1). The waveguides could be realized by means of standard lithography using e.g. Germanium on insulator substrates (GOI). The Ge waveguide cross-section is chosen to be 550 nm wide and 220 nm height. The silica layer substrate has been chosen to maximize the refractive index contrast for an optimal light confinement, while maintaining CMOS compatibility. On top of both the straight sections of the interferometric arms, whose longitudinal axes are aligned along the (100) crystallographic direction (*x* axis), a piezoelectric stressor material is deposited in order to electrically control the lattice deformation of the underlying WGs. Each stressor is sandwiched between two electrical contact layers (see inset of Fig. 1). To reduce the related optical losses, in our simulations we have considered as contact material thin (50 nm) $n^{++}$ polysilicon layers, which are compatible with standard CMOS processing. The description of a similar fabrication process, aimed to the realization of integrated wave guide Ge detectors, can be found in [16].

As a stressor material we have chosen a 150 nm–thick epitaxial $Pb(Zr,Ti)O_3$ (PZT) layer, due to its superior piezoelectric properties [17] and compatibility with Si technology [18]. Moreover, the low refractive index of PZT [19] is beneficial for mode confinement in the underlying Ge WGs. PZT is also relatively immune to temperature changes, and this would add robustness to the device [20].

The phase mismatch mechanism which governs the intensity of the output light is tuned by a controlled variation of the WG refractive index. This is obtained by inducing a proper change in the Ge band structure driven by the lattice deformation induced by a PZT stressor, as will be clarified in the following sections. The interferometer structure was simulated with Finite Element Method (FEM) using CMOSOL 4.2(a). The strain field in the germanium WGs was calculated using the structural mechanics environment of COMSOL, while piezoelectric module was used for the analysis of the PZT actuator. Both the modules were coupled in the multi-physics environment and were run simultaneously [21]. A "*fixed*" boundary condition was chosen for the bottom of the $SiO_2$ substrate while all the other surfaces were left "*free*" to relax.

#230620 - $15.00 USD Received 11 Dec 2014; revised 30 Jan 2015; accepted 4 Feb 2015; published 25 Feb 2015
© 2015 OSA

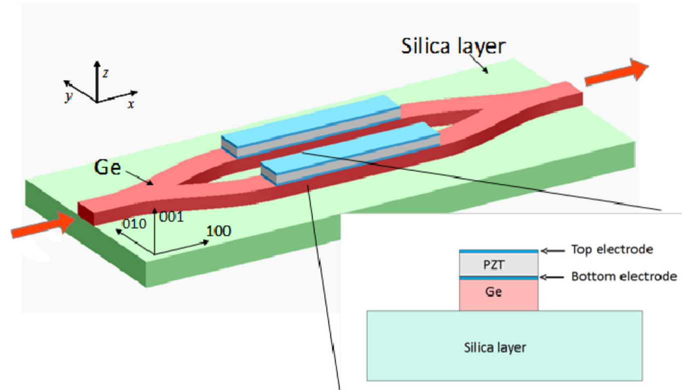


Fig. 1. Scheme of the proposed case-study device given by a MZI structure built on a GOI substrate also showing the CMOS-compatible piezoelectric stressor elements on top of MZI arms and the crystallographic orientation of the device layer. Inset: cross-sectional schematics of MZI arm structure including PZT actuator: the waveguide width is 550 nm while its height is 220 nm. The 150 nm-thick piezo stressor is sandwiched between 50-nm thick poly-silicon electrodes.

As a first simulation step, a stationary analysis was carried out to elucidate the actuation principle with different bias voltages applied to the contact electrodes. Differential voltages in the range of 0 to 10 V have been simulated and the corresponding uniaxial strain at the interface of germanium and the piezo-actuator was calculated. Subsequently, simulations in the frequency domain were carried out in order to calculate the maximum switching speed of the device. The switching speed is set by the first eigen-frequency of the piezo-actuator, related to its geometry.

The optical material properties of the strained Ge material have been modeled starting from their electronic band structure as calculated by means of a ***k·p*** multi valley effective mass approach [22]. The adopted model relies on a parabolic approximation and consider the presence of the heavy hole (HH), light hole (LH), and split-off (SO) bands in the valence and of the $L_c$, $\Gamma_c$ valleys in the conduction. Strain effects on the band edges have been incorporated in the calculations within the framework of the deformation potential theory. Absorption spectra have been evaluated taking into account direct and indirect transitions which involve the HH, LH, and SO bands. To this aim polarization and strain dependent dipole matrix elements obtained by means of tight-binding calculations [23] have been used.

For the optical analysis, the vectorial Helmholtz equation for the interferometer cross section has been solved. The complex refractive index of the Ge, as calculated by the ***k·p*** method, has been used as input parameter. The Helmholtz equation has been solved using a FEM analysis [24], with perfectly matched layer absorbing boundary conditions at the simulation domain boundaries. As a result, the complex propagation constants for the waveguides were obtained, and, upon using a transfer matrix method, the insertion losses (IL) and extinction ratios (ER) have been evaluated. In order to better highlight the performance of the proposed modulation mechanism, we considered the light propagation through the straight arms of the interferometer only, while the losses related to the Y-splitters (due to scattering and absorption) have been neglected.

### 3. Finite elements analysis of the electrically induced lattice deformations

In Figs. 2(a) and 2(b) we display the distribution of the $\varepsilon_{yy}$ strain values, obtained for a *yz* section located at the center of one of the MZI arm, for a positive ( + 3V, initial configuration) and negative (−3V, final configuration) bias, respectively, i.e. for a ΔV = 6V voltage swing. Notice that the reference values for the strain tensor in the PZT correspond to the condition of full volume relaxation. When the PZT is positively biased, the resulting

#230620 - $15.00 USD Received 11 Dec 2014; revised 30 Jan 2015; accepted 4 Feb 2015; published 25 Feb 2015
© 2015 OSA

tensile deformation along the perpendicular $z$ direction is associated to a contraction in the parallel plane, which is contrasted by the underlying Ge WG. As a result in Ge we have $\varepsilon_{yy}$<0. For what concerns $\varepsilon_{xx}$, its magnitude in the Ge region is ~0, owing to the impossibility of release the elastic energy along the longitudinal axis. This feature can be observed in Fig. 2(c), where we display the values of the three diagonal components of the strain tensor calculated in Ge for ± 3V biases at its interface with PZT for $y = 0$ and as a function of $x$ (stressor length $L = 25$ µm). The strain distribution of $\varepsilon_{zz}$ in Ge is essentially determined by its off-diagonal elastic constants. For a positive bias it results to be positive, in accordance to the fact that $\varepsilon_{yy}$<0. Moreover the $\varepsilon_{zz}$ magnitudes are smaller than those of the corresponding $\varepsilon_{yy}$.

The strain distribution shown in Fig. 2(c) is highly homogeneous along the entire stressor length and, as evidenced by the data shown in panel a), a quite good spatial homogeneity of the strain distribution of Ge is obtained also in the $y$ direction for a given $z$ value. For the opposite bias (−3V) the strain distribution is inverted [see Figs. 2(b) and 2(c)], with tensile (compressive) $\varepsilon_{yy}$ ($\varepsilon_{zz}$) strain in Ge, with $\varepsilon_{xx}$~0. From the above considerations it follows that the tensor trace is negative and positive for positive and negative applied bias, respectively.

The "swing" of the uniaxial strain $\varepsilon_{yy}$(-V) - $\varepsilon_{yy}$( + V) calculated at the Ge WG top surface is displayed in Fig. 2(d), showing a linear dependence on ΔV. Notice that for ΔV = 10 V the uniaxial strain swing in the structure can reach values in excess of 1%.

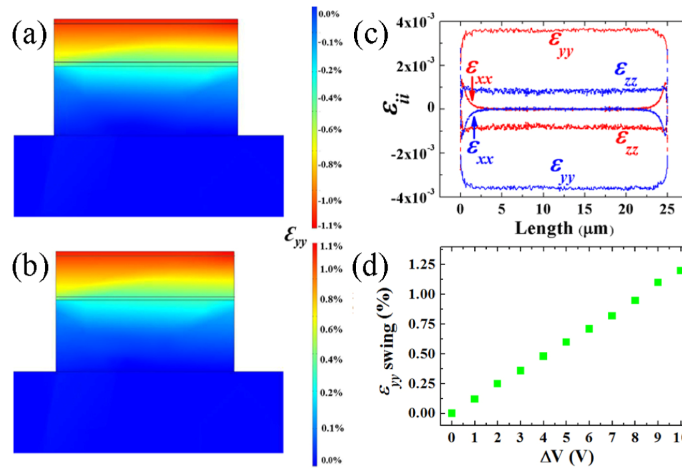


Fig. 2. Distribution of $\varepsilon_{yy}$ values, obtained for a $yz$ section located at the center of one of the MZI arm, for a positive ( + 3V, panel (a)) and negative (−3V, panel (b)) bias. (c): Diagonal components of the strain tensor, calculated in Ge at the PZT/Ge interface for $y = 0$ with a + 3V bias (blue curves) and −3V bias (red curves) and plotted as a function of the distance along the center axis structure ($x$-axis). (d) $\varepsilon_{yy}$ swing in Ge at the PZT/Ge interface ($y = 0$), as function of the bias difference ΔV applied to the PZT stressor.

Finally, we point here out that the off-diagonal tensor elements results to be negligible in all the investigated cases.

For the given geometry of the structure, the maximum switching speed calculated was 250 MHz, corresponding to a single ended operation where one electrode is biased while the other electrode is grounded. The $\varepsilon_{yy}$ component of the strain is approximately constant for the entire switching frequency spectrum. The energy required for switching was calculated using post processing techniques to be 400 fJ/cycle at the maximum switching frequency. Note that the 250 MHz limit refers to the frequency of switching/refractive index variations induced on light wave signals. Nonetheless, the bandwidth of the processed signals can be very high, thanks to the inherent transparency of the proposed mechanism to modulation format and bit rates, since optical properties of employed semiconductor materials do not vary significantly for signal carriers whose bandwidths are extending well over 100 GHz. The 250 MHz

#230620 - $15.00 USD Received 11 Dec 2014; revised 30 Jan 2015; accepted 4 Feb 2015; published 25 Feb 2015
© 2015 OSA

frequency would indeed constitute a limit for the use of MZI as a modulator (data rates for optical channel currently exceed 10Gb/s and aim at 100 Gb/s and beyond). However this switching speed enables the use of the proposed approach in optical switching devices, to be employed when switching rates can be significantly lower, e.g. in circuit-switching architectures.

**4. Strain induced variation of the refractive index**

In order to understand the physical mechanism underlying the stressor-induced refractive index variations, we discuss here the effects of the strain field on the band structure of the Ge WG. To this aim we first remind that at room temperature the direct gap in bulk Ge across the Γ point, is at about 800 meV (1.550 μm) while the absolute minimum in the conduction band occurs at the fourfold degenerate L points, which are 134 meV only lower in energy than the $\Gamma_c$ conduction valley minimum. As previously discussed, when the PZT is extended along $z$ (V>0) $\varepsilon_{yy}$ is negative and, since its modulus is larger than $\varepsilon_{zz}$, which is positive, the tensor trace results to be negative. The related strain-induced shifts of the barycenter of the HH, LH, and SO valence bands and of the $\Gamma_c$ and $L_c$ conduction energy extrema are proportional to the strain tensor trace, multiplied by the relative deformation potentials [22]. Notice that the $L_c$ valleys fourfold degeneracy is preserved by the uniaxial strain perturbation because the tetragonal symmetry is not broken due to the chosen waveguide orientation (see Fig. 1). For V>0 the valence and conduction band deformation potentials are such that both the direct $E_{dir}$ and indirect $E_{ind}$ gaps increase. At a positive bias of + 3V we obtain the following values for the diagonal components of the strain tensor: ($\varepsilon_{xx}$, $\varepsilon_{yy}$, $\varepsilon_{zz}$) = (0, −0.36%, 0.08%). The related shift of the band edges can be seen from Fig. 3(a) (blue lines) by comparison with the energy levels of cubic Ge (black lines). When the bias is reversed (−3V) $\varepsilon_{ii} \rightarrow -\varepsilon_{ii}$ and the gaps decrease as shown in Fig. 3(a) (red lines). The absorption spectra calculated at zero bias and at ± 3V are displayed in Fig. 3(b), from which is apparent the blue (red) shift of both the direct and indirect absorption edges induced by the positive (negative) applied bias.

As it can be seen in Fig. 3(c) for photon energy above the fundamental gap, the switch of the applied bias from 3V to −3V entails a positive variation of the absorption coefficient $\Delta\alpha(\omega) = \alpha_{-3V}(\omega) - \alpha_{+3V}(\omega)$, with much larger values predicted for $\eta\omega > E_{dir}$.

In principle, this kind of strain-driven variation of the absorbance could be exploited in an electro-absorption modulator operating at wavelength close to the direct absorption edge. However, as we have shown before, for realistic values of the bias applied to the stressor, the strain variation in the parallel plane is less than ~0.5%. Considering the related changes in the absorption coefficient, it follows that for a reasonable device length the operation photon energy must lay well inside the indirect absorption region, also when the system is in the transparency condition. As a consequence, the device would suffer from limited modulation depth and high insertion losses. To overcome this limitations, the same strain-driven modulation of $\alpha(\omega)$ can be used in interferometric devices operating below the indirect absorption edge. In fact, the variation of $\alpha(\omega)$ obtained in the energy region close to the absorption edges is associated to a strong change of the real part of the refractive index $n_1(\omega)$, which remains robust also at photon energies well below the fundamental gap. This effect can thus be exploited to tune the phase mismatch between the light waves travelling in the two MZI arms at frequencies below the indirect absorption edge i.e., in the transparency windows of the waveguide material.

#230620 - $15.00 USD Received 11 Dec 2014; revised 30 Jan 2015; accepted 4 Feb 2015; published 25 Feb 2015
© 2015 OSA

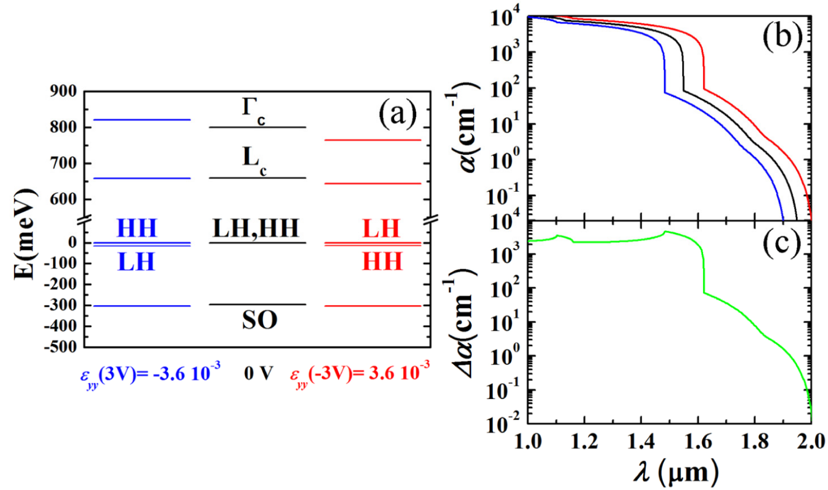


Fig. 3 . (a) Energy band edges for strained (001)-Ge calculated for a positive (blue lines) and negative (red lines) bias of 3V applied to the PZT stressor. Band edges at zero bias, corresponding to relaxed Ge are also shown (black lines). The zero-energy point has been set at the topmost valence band edge in all the cases. Notice the lifted degeneracy of the HH and LH valence bands. (b) Corresponding TM absorption spectrum obtained by means of $\boldsymbol{k}\cdot\boldsymbol{p}$ calculations which include also indirect transitions. Notice that in this case, HH-related transitions are not active. (c) Differential absorption $\Delta\alpha(\omega)$ evaluated from data of panel (b) corresponding to a ± 3V bias switch.

For a given polarization state of the propagating light (TE or TM), the variation of the refractive index $\Delta n_1(\omega)$ can be estimated from $\Delta\alpha(\omega)$ via the Kramers-Kronig (KK) transformation as [25]

$$\Delta n_1(\omega) = \frac{c}{\pi} P\int_0^\infty \frac{\Delta\alpha(\omega')d\omega'}{\omega'^2-\omega^2} \tag{1}$$

Notice that the polarization dependence of the $\Delta n_1(\omega)$ and $\Delta\alpha(\omega)$ in Eq. (1) is due to the non-cubic symmetry of the strained waveguide material. In fact the strain on the material induces refractive index anisotropy, and a consequent polarization-dependent waveguide birefringence.

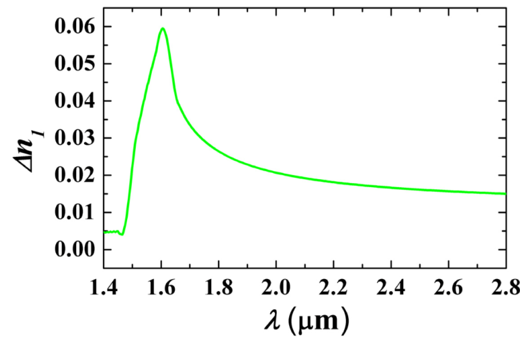


Fig. 4. Variation $\Delta n_1$ for the real part of the refractive index as function of the wavelength, obtained for TM polarization and with a voltage swing of 3V→-3V of the bias applied to the stressor layer.

In Fig. 4 we display the spectral dependence of $\Delta n_1(\omega)$ for the TM mode and for an applied swing from 3V to −3V. The predicted $\Delta n_1(\omega)$ values are in the $6 \times 10^{-2} - 1.5 \times 10^{-2}$ interval for wavelengths λ in the 1.6 – 2.5 μm range. To make a comparison, such high values can be achieved in conventional Si-based MZI devices based on free carrier injection, only for carrier densities in excess of $10^{19}$ cm$^{-3}$. At such ultra-high concentrations the device

#230620 - $15.00 USD Received 11 Dec 2014; revised 30 Jan 2015; accepted 4 Feb 2015; published 25 Feb 2015
© 2015 OSA

performance drops due to large free carrier absorption of light. On the contrary, the approach proposed here allows one to achieve large refractive index variations without compromise with increased optical losses, thus permitting to design very compact devices with low insertion losses. In fact, as shown in Sec. 5, the π dephasing length for operating wavelengths in the whole 1.6–2.5 μm range result to be $L_\pi$<25 μm. We notice that a further advantage of the proposed solution is given by the broad design flexibility associated with the wide spectral extension of $\Delta n_1(\omega)$.

## 5. Photonic simulations of MZI structure

We have performed electromagnetic simulations on the simple MZI case-study depicted in Fig. 1, where the refractive index variations are induced by alterations of band structure due to strain. The study has been carried out for a wavelength λ = 1700 nm. This particular wavelength has been chosen because it is the targeted operating wavelength of an integrated Ge laser under development by our group [26]. As can be observed from Fig. 4, the effect of the strain field extends over a relatively broad spectrum and other wavelengths could be alternatively used.

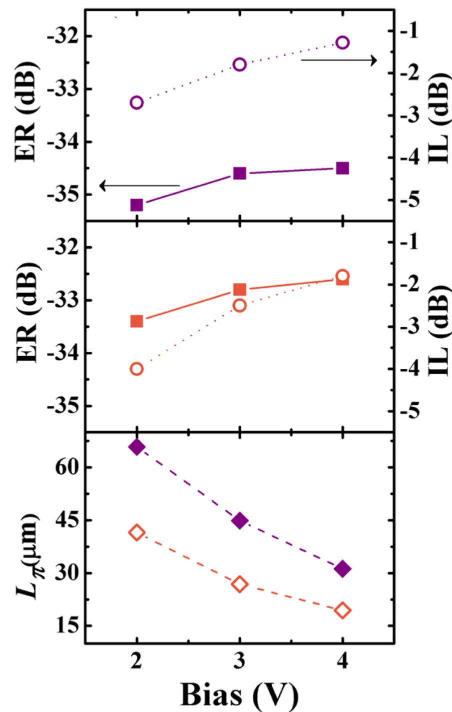


Fig. 5. Extinction ratio (solid symbols, left axis) and insertion loss (open, right axis) for the MZI operated at different PZT bias, for the fundamental TE (top panel), and TM (center panel) mode. In the bottom panel we show the length of the active region $L_\pi$ for the fundamental TE mode (closed symbols) and TM mode (open).

The metal electrodes have been included in the photonic simulation as highly $n^{++}$-doped poly-silicon material with a refractive index of $n_l$ = 3.3 and an absorption coefficient value of 3500 $cm^{-1}$. The employed refractive indices at λ = 1700 nm of silica and PZT layers are 1.442 and 2.3, respectively.

The complex propagation constant in the straight waveguide section is calculated for both arms of the MZI, considered as not interacting [27]. The design of the Y-coupler (length, bending angle, arm distance) does not enter the calculations. The extinction ratio is extracted

#230620 - $15.00 USD Received 11 Dec 2014; revised 30 Jan 2015; accepted 4 Feb 2015; published 25 Feb 2015
© 2015 OSA

from the interference of the fundamental TE/TM modes after propagation for a length $L$ in the two arms.

The Ge active layer of the waveguide has an optical confinement factor of 75-80% for the fundamental TE/TM modes, depending on the operation voltage. The refractive index and absorption coefficient of the strained Ge layer are calculated with the two arms biased oppositely and for bias values in the 2-4 V range, i.e. for bias swings in the 4-8 V range. The related optical constant values have been obtained from the band structure calculations of Sec. 4, and are reported in Table 1 for both TE and TM modes. The insertion loss results from the propagation loss of the waves travelling the distance $L$ in the MZI arms.

**Table 1. Optical parameters for strained germanium derived from band structure calculations shown as a function of the PZT stressor bias (λ = 1700 nm)**

| | TE | | TM | |
|---|---|---|---|---|
| Bias (V) | $n_l$ | $\alpha$ (cm$^{-1}$) | $n_l$ | $\alpha$ (cm$^{-1}$) |
| –4 | 4.190 | 35.1 | 4.205 | 58.2 |
| –3 | 4.186 | 29.8 | 4.196 | 43.5 |
| –2 | 4.182 | 25.5 | 4.188 | 32.3 |
| 0 | 4.175 | 19.2 | 4.175 | 19.2 |
| + 2 | 4.170 | 14.9 | 4.166 | 9.5 |
| + 3 | 4.168 | 13.3 | 4.162 | 6.7 |
| + 4 | 4.165 | 12 | 4.158 | 4.9 |

Figure 5 shows the calculated ER and IL for the fundamental TE mode (top panel) and TM mode (center) of the MZI. The calculations have been carried out for a MZI arm length that matches the π-shift length $L_\pi$ at the considered bias voltages. The predicted values for $L_\pi$ are reported in the bottom panel for both TE and TM mode. The obtained ERs are larger than –30dB even for voltage swings as low as ± 2 V. The IL increases upon lowering the voltage swing, as the absorption losses increase with the device getting longer. The IL values for the TE mode are much lower than for the TM one, due to a larger mode overlap with the absorptive poly-silicon contact in the latter case. For a bias swing of ± 4 V, the arms are shorter than 40 µm (see Fig. 6). The lengths corresponding to the TM mode are smaller due to the improved field confinement factor within the waveguide, and to the larger modulation of the refractive index at a given bias. This allows for $V_\pi L_\pi$ values as low as ~0.015 Vcm.

Scattering losses at the waveguide sidewalls and in the poly-Si material can be estimated and added to the IL of Fig. 5, by taking in to account mode overlaps in the different regions of the device. The optical confinement factor of the poly-Si layers is 3%, and typical active lengths of the MZI arms are 50 µm. This adds a loss to the system of 0.5 dB. Also, if we consider the sidewall scattering losses of the Ge waveguide (measured to be 0.3 dB/cm on similar structures [16]) on a length of 250 µm (MZI and a typical Y-coupler length) an additional contribution to losses of 0.75 dB can be estimated. Therefore, these scattering losses may increase by ~1.25 dB the IL reported in Fig. 5.

Finally, to investigate how short the active region can be made while still maintaining a reasonable ER, we have reduced the length of the active region from its π-shift length value $L_\pi$, at a fixed bias value. Figure 6 shows the IL and ER for the TM mode at $\lambda$ = 1700 nm wavelength as a function of the arm length $L$. Starting from the initial π-shift value $L_\pi$ = 19.4 µm (obtained for V = ± 4V), the length is reduced and a dramatic decrease of ER due to the loss of destructive interference is consequently observed. However, for values of the ER similar to those obtained in electro-absorption modulator (–10 dB) [1], the device length can be as small as ~14 µm. This result, together with the much lower losses achievable (~-1 dB),

#230620 - $15.00 USD Received 11 Dec 2014; revised 30 Jan 2015; accepted 4 Feb 2015; published 25 Feb 2015
© 2015 OSA

makes our proposed approach a good candidate for ultra-compact interferometers or optical switches, where refractive index variation is accomplished in a waveguide region of 15-20 μm length and 0.5 μm width, with an expected overall form factor of the element of about 100-300 $\mu m^2$.

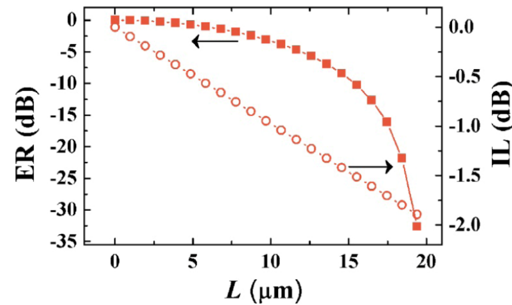


Fig. 6. Extinction ratio and insertion loss for different active lengths of the MZI, calculated for the TM mode at 1700 nm and for V = ± 4V.

## 6. Conclusions

In conclusion, we have proposed a mechanism which is capable to induce significant refractive index variations through application of material strain in a CMOS compatible Si-photonics platform, resulting in very compact devices and having a broad range of applications, from basic signal processing to optical switching in telecom and datacom networks. This mechanism is based on band structure modification through application of an electrically induced strain. The feasibility of the proposed mechanism has been then numerically assessed in a detailed case-study given by a MZI based on GOI WG and PZT stressors and operating at wavelengths near the indirect absorption edge of the waveguide material. Finite-element strain modelling, together with electronic band structure calculations and electromagnetic field analysis, predict, for moderate PZT electrical bias, a significant refractive index change of the order of $\sim 5 \cdot 10^{-2}$ at 1700 nm with switching rates up to 0.5 GHz and inherent bit-rate and modulation-format transparency. The corresponding π dephasing length is found to be as short as $L_\pi \sim 20$ μm, the insertion loss IL < 4 dB, and the extinction ratio ER>30 dB. Therefore the proposed device could outperform the specifications of existing integrated-photonic devices.

Finally we point out that the proposed method could also be applied to SiGeSn waveguide to achieve longer operational wavelength and to Ge-rich SiGe waveguides if shorter operation wavelengths (e.g. in the 1550 nm range) are targeted.

#230620 - $15.00 USD Received 11 Dec 2014; revised 30 Jan 2015; accepted 4 Feb 2015; published 25 Feb 2015
© 2015 OSA